Computer Assisted Mechanics and Engineering Sciences, 7: 23–37, 2000.

Steady 3D incompressible flow analysis for the simplified train–tunnel interaction

Sungcho Kim
Department of Mechanical Engineering, College of Engineering, Sunchon National University, 315 Maegokdong, Sunchon, Chonnam 540-742, Korea

Bharat K. Soni
NSF Engineering Research Center for Computational Field Simulation, Mississippi State University, MS 39762, USA

(Received January 28, 1999)

This paper describes the phenomena that occur when a simplified model of train interacts with the tunnel at three locations – before, entering and leaving the tunnel. The Navier–Stokes equation is solved by introducing the artificial compressibility to change the governing equation type from the elliptic to hyperbolic. The Baldwin–Lomax turbulence modeling is employed to simulate the flow field with a Reynolds number of 10^6 , and the computation domain is divided into three blocks considering the train and tunnel geometries. The grid is algebraically adapted determining the maximum solution change plane and solution weighting factors. The pressure in the adapted solution is not changed much, however, the skin friction is severely varied comparing with those of the non-adapted solutions. When the train enters into the tunnel, there are large increase in the surface pressure and skin friction distribution on the train surface.

1. Introduction

The surface train is still important in view of the passenger and cargo transport, and its maximum speed will have been increased from 100 km/h in 1920's to more than 500 km/h in the near future. It is very interesting and practically essential to understand the flow field around the train, ad hoc, when it dashes into or comes out of the tunnel because the unbalanced substantial aerodynamic forces affect the traveling stability. For example, the speed and relative position to the ground of the high speed train floated and driven by the magnetic force should be controlled accurately, and thus it is inevitable to decide and to construct the optimal tunnel geometry since there may be a severe pressure on the surface change when a train moves into a tunnel especially.

There are little experiments for the flow field around the train running into the tunnel due to the difficulties of the measuring data. Theoretical [29] and computational analysis [16] investigated one- or two-dimensional inviscid compressible flow induced by the high speed, respectively. Ogawa and Fujii [16] treated two-dimensional moving train for compressible flow with changing the train length. Swarden [23] presented the experimental results for vehicle tunnel entry at subsonic speed, of which geometry is simple axi-symmetric, and Aita *et al.* [1] investigated the train-tunnel unsteady aerodynamics experimentally and numerically using the finite element method. Even though they did not mention the turbulence modeling and the moving grid, the research is valuable because the realistic train geometry is treated. It is highly complicated and needs large memory storage and computation time to solve the unsteady three-dimensional real flow field around the train moving into the tunnel. Especially when the flow field is compressible there are similar complex pressure distributions at the front and rear parts of the train regardless of its relative location to the tunnel [16]. The behavior of flow fields in the train-tunnel problem is strongly dependent on the

parameters such as the tunnel geometry, blockage ratio (cross-sectional area ratio between tunnel and train), ground effect, train geometry, train speed, etc. The grid system around nearly real shape of train and simple tunnel was conceptually generated by Casella *et al.* [7], however, they did not calculate the flow field and the grid quality is not good.

In this paper, it is focused to calculate the basic flow phenomena for the steady state three cases according to the relative location of train to the tunnel, i.e., when it runs towards, begins to enter and leave the tunnel, respectively. The highest speed of modern trains is in the range less than Mach number 0.3, thus the total flow field can be considered as incompressible. That is, the local compressibility is neglected in this analysis. The Reynolds number is chosen to be 10^6 based on the tunnel diameter and the blockage ratio is 4. Both the cross-sections of tunnel and train are semi-circle and both the head and tail of the train are same quarter spheres. The train-tunnel flow is considered to be a kind of internal (inside the tunnel) and external (outside the tunnel) flow, and these different flow regimes are treated by the multi-block method. In addition, the grid is adapted by the algebraic method to improve the solution.

2. Governing equations

2.1. In Cartesian coordinates

The unsteady three-dimensional viscous flow is governed by the Navier–Stokes equation, which has three kinds of types – elliptic, parabolic and hyperbolic – depending on the flow states, i.e. incompressible or compressible. The pressure term plays a role of a dynamic parameter in the governing equations and needs to be treated specially. If the artificial (or pseudo-) compressibility is introduced, which Chorin [10] and other researchers proposed to reduce the large computation time required to realize the divergence free condition, the steady state incompressible Navier–Stokes equation can be solved effectively in a similar ways used for the compressible flow solver [8]. Basically, this concept introduces the finite wave speed into the incompressible flow fields to distribute the pressure, and the propagation speed of pseudo-waves directly depends on the magnitude of the pseudo-compressibility. It is important to choose the proper value of the pseudo-compressibility to obtain the desired solution, which is a function of the flow characteristics. Since the wave speed depends on the pseudo-compressibility, it must be chosen carefully when the boundary layer is separated. For example, if the pressure fields oscillate due to the finite speed waves, the separation points may fluctuate accordingly. Now the continuity equation is modified by adding the time derivative of pressure based on the artificial compressibility concept as below to result in a hyperbolic system

$$\frac{1}{\beta}\frac{\partial p}{\partial t} + \frac{\partial u_i}{\partial x_i} = 0, \tag{1}$$

where β is the artificial compressibility constant and should be chosen according to a Reynolds number and characteristic length of the geometry through the wave propagation analysis [8, 19]. Theoretically, β should be chosen to guarantee the incompressible flow state. Otherwise this may contaminate the solution accuracy and the numerical stability. For example, if β is too small, the boundary layer will not be developed properly. Therefore, the speed of the pressure wave should be controlled and chosen to avoid the interactions with the vorticity spreading. In this research, the optimal value of β is determined to be 10.

And using with the time averaged primitive variables and constant density, the Navier–Stokes equation becomes

$$\frac{\partial u_i}{\partial t} + \frac{\partial u_i u_j}{\partial x_j} = \frac{1}{\rho}\left[-\frac{\partial p}{\partial x_i} + \frac{\partial \tau_{ij}}{\partial x_j}\right], \tag{2}$$

where τ_{ij} is the viscous stress tensor and can be simply expressed by the eddy viscosity model as

$$\tau_{ij} = (\mu + \mu_t)\left(\frac{\partial u_i}{\partial x_j} + \frac{\partial u_j}{\partial x_i}\right). \tag{3}$$

By nondimensionalizing all of the physical variables by a reference velocity and length, the combination of Eqs. (1) and (2) has the conservative form of

$$\frac{\partial D}{\partial t} + \sum_{i=1}^{3} \frac{\partial (F_i - F_{vi})}{\partial x_i} = 0, \tag{4}$$

where D is the conserved (physical) variables vector, F_i the component of convective flux vectors, and F_{vi} the component of viscous flux vectors, i.e.,

$$D = \begin{bmatrix} p \\ u \\ v \\ w \end{bmatrix}, \qquad [F_i] = \begin{bmatrix} \beta u_i \\ u u_i + \delta_{1i} p \\ v u_i + \delta_{2i} p \\ w u_i + \delta_{3i} p \end{bmatrix}, \qquad [F_{vi}] = \begin{bmatrix} 0 \\ \tau_{1i} \\ \tau_{2i} \\ \tau_{3i} \end{bmatrix}.$$

2.2. In general curvilinear coordinates

In order to calculate the general three-dimensional flow field around an arbitrary geometry, it is necessary to transform the physical coordinates into the general curvilinear ones as follows

$$\tau = t, \qquad \xi_i = \xi_i(x, y, z), \qquad \xi_{i_{x_i}} = J(x_{j_{\xi_j}} x_{k_{\xi_k}} - x_{j_{\xi_k}} x_{k_{\xi_j}}), \qquad \text{etc.},$$

where J is the Jacobian of the transformation. Thus the final difference form of the conservative Eq. (4) becomes

$$\delta_\tau \hat{D} + \sum_{i=1}^{3} \delta_{\xi_i} (\hat{F}_i - \hat{F}_{vi}) = 0. \tag{5}$$

where $\hat{}$ means the vectors in transformed coordinates and δ the finite difference and

$$\hat{D} = J^{-1} D, \qquad \hat{F}_i = J^{-1}[(\xi_i)_t D + \sum_j (\xi_i)_{x_j} F_j], \qquad \hat{F}_{vi} = J^{-1} \sum_j (\xi_i)_{x_j} F_{vj}.$$

2.3. Numerical procedure

Equation (5) can be solved by the implicit, noniterative, approximately factorized and finite difference scheme. The difference for time with second order accuracy is expressed by the trapezoidal rule [4, 5]

$$\delta_\tau \hat{D} = \frac{1}{2}\left(\delta_\tau \hat{D}^{n+1} + \delta_\tau \hat{D}^n\right) + O(\Delta\tau^2) \tag{6}$$

where the superscript n and $n+1$ mean the time step and Δt is its size.

The convected flux vectors which are the nonlinear function should be locally linearized using the Taylor series expansion [8, 19]

$$\hat{F}_i^{n+1} = \hat{F}_i + \frac{\partial \hat{F}_i^n}{\partial \hat{D}} (\hat{D}^{n+1} - \hat{D}^n) + O(\Delta\tau^2), \tag{7}$$

where $\partial \hat{F}_i / \partial \hat{D}$ is the Jacobian matrices and denoted by $\hat{A}_i$ from now on. To write the viscous flux vector as the function of the physical variables vector, it is assumed that the coordinate system is orthogonal, viscosity is constant and the velocity field is divergence-free, then

$$\hat{F}_{vi}^{n+1} = (\nu + \nu_t) J^{-1} \nabla \xi_i \cdot \nabla \xi_i \, \mathrm{Im} \frac{\partial \hat{D}^{n+1}}{\partial \xi_i} = \Gamma_i \hat{D}^{n+1}, \tag{8}$$

where $\mathrm{Im} = [i_{ij}]$, $i_{ij} = \delta_{ij}$ and $i_{11} = 0$.

The Jacobian matrices defined above is finally rearranged as

$$\hat{A}_i = \frac{1}{J} \begin{bmatrix} L_0 & L_1\beta & L_2\beta & L_3\beta \\ L_1 & Q + L_1 u & L_2 u & L_3 u \\ L_2 & L_1 v & Q + L_2 v & L_3 v \\ L_3 & L_1 w & L_2 w & Q + L_3 w \end{bmatrix},$$

where Q is the contravariant velocity, L_0 the grid speed and L_j the metrics, i.e.,

$$Q = L_0 + \sum_i L_i u_i \,, \qquad L_0 = (\xi_i)_t \,, \qquad L_j = (\xi_i)_{x_j} \,.$$

Substituting Eqs. (6) and (7) into Eq. (5), the linearized system in delta form can be obtained,

$$\left[I + \frac{h}{2} J^{n+1} \sum \delta_{\xi_i} (\hat{A}_i^n - \Gamma_i) \right] (\hat{D}^{n+1} - \hat{D}^n)$$

$$= -\Delta\tau J^{n+1} \left[\sum \delta_{\xi_i} (\hat{F}_i - \hat{F}_{vi})^n \right] + \left(\frac{J^{n+1}}{J^n} - 1 \right) \hat{D}^n = RHS, \tag{9}$$

where $h = \Delta\tau$ (trapezoidal scheme), or $2\Delta\tau$ (Euler's scheme).

Since it is very difficult to solve Eq. (9) directly, approximate factorization scheme is adopted, i.e., Eq. (9) can be splitted to use a multi-stage one-dimensional inversion scheme such as ADI(alternating direction implicit) method, which can be effectively solved by the well-known Thomas algorithm. Thus Eq. (9) is approximately factorized with second order central differencing and finally comes to get the 3 block tridiagonal matrices. That is, Eq. (10) can be solved through three-stage ADI method using a block LU (lower-upper triangular) decomposition procedure,

$$\prod_{i=1}^{3} L_{\xi_i} (\hat{D}^{n+1} - \hat{D}^n) = RHS, \tag{10}$$

where

$$L_{\xi_i} = \left[I + \frac{\Delta\tau}{2} J^{n+1} \delta_{\xi_i} (\hat{A}_i^n - \Gamma_i) \right],$$

and I is a unit matrix.

It is necessary to introduce the diagonal algorithm in order to solve Eq.(10) more efficiently with the reduced calculation time, which diagonalizes the Jacobian matrices into the similarity form and converts Eq.(10) into the uncoupled one [14, 17, 26, 27]. The block tridiagonal matrices are changed to the scalar ones, and there is a similarity transformation which makes the Jacobian matrices to be diagonalized such as

$$\hat{A}_i = T_i \hat{\Lambda}_i T_i^{-1},$$

where $\hat{\Lambda}_i$ is a diagonal matrices consisting of the eigenvectors T_i of the Jacobian matrices, i.e.,

$$\hat{\Lambda}_i = \frac{1}{J} \begin{bmatrix} Q & 0 & 0 & 0 \\ 0 & Q & 0 & 0 \\ 0 & 0 & Q + C & 0 \\ 0 & 0 & 0 & Q - C \end{bmatrix}$$

and C is the pseudo-speed of sound defined by

$$C = \sqrt{(Q - L_0)^2 + \beta \sum L_i^2}$$

due to the artificial compressibility. T_i is derived in detail in [17] and its determinant is a function of a kind of pseudo-speed of sound. The linear, implicit and differential operator is changed to the following form in a similar ways applied to the Jacobian matrices,

$$L_{\xi_i} = T_{\xi_i} \left[I + \frac{\Delta\tau}{2} J \delta_{\xi_i} (\hat{\Lambda}_i - \hat{\Gamma}_i) \right] T_{\xi_i}^{-1},$$

where $\hat{\Gamma}_i = (\nu + \nu_t) J^{-1} \nabla\xi_i \cdot \nabla\xi_i \, I \delta_{\xi_i}$.

Meanwhile, the implicit approximate factorization and diagonalization algorithm make the solution unstable due to the higher order oscillations because the second-order central differencing is used for the space. This phenomena is serious in the calculation of high Reynolds number flows. Thus some kinds of smoothing (or dissipation) term should be added to Eq. (10) to dissipate the undesirable oscillation. In general, the following second- or fourth-order artificial dissipation term is used.

$$(\nabla_x \Delta_x)^2 u = \frac{1}{4\Delta x}(u_{j-2} - 4u_{j-1} + 6u_j - 4u_{j+1} + u_{j+2}),$$

$$\nabla_x \Delta_x u \quad = -\frac{1}{2\Delta x}(u_{j+1} - 2u_j + u_{j-1}).$$

Thus *RHS* in Eq. (10) and the differencing operator are modified respectively by introducing the numerical dissipation,

$$\begin{aligned} &RHS \longrightarrow RHS - \varepsilon_E [\Sigma(\nabla_{\xi_i} \Delta_{\xi_i}^2)] \hat{D}^n, \\ &L_{\xi_i} = \left[I + \frac{\Delta\tau}{2} J^{n+1} \delta_{\xi_i} (\hat{A}_i^n - \Gamma_i) - \varepsilon_I \nabla_{\xi_i} \Delta_{\xi_i} \right], \end{aligned} \tag{11}$$

where ε_E, ε_I are the smoothing coefficients depending on the Reynolds number and grid size [9, 15].

2.4. Boundary conditions

In this research, the flow field is divided into three blocks. No-slip condition is applied on the solid surfaces or walls, the pressure gradient normal to the solid surface is assumed to be zero, the inflow velocity is simply specified uniform without regard to cases, and the physical variables on the other boundaries are calculated by the extrapolation to implement new boundary conditions. Data on the block boundaries is interactively transferred, and the symmetric condition is adopted on the symmetric (or central) surface in the way that there is no cross-flow velocity components through that surface, while the Neumann condition is applied on the far boundaries.

2.5. Turbulence modeling

There seems to be no results that the algorithms adopted the artificial compressibility can successfully handle the widely used $k - \varepsilon$ turbulence modeling. In most cases of engineering, even an algebraic turbulence modeling has predicted the flow field pretty well. Therefore the mixing length theory for turbulence modeling known as Baldwin–Lomax model [3] is used, where the turbulence viscosity is evaluated based on the vorticity magnitude.

3. Grid system

The simple geometries used in this research consist of the tunnel and train, which are half circular cylinder with radius R and 1/4 sphere (nose) + half circular cylinder (main body, $r = 0.5R$)+1/4 sphere (tail), respectively. It is assumed that the train runs toward the tunnel from right to left. The tunnel length is $3R$ and the train length (L_t) $2R$. The calculations are executed for the distinct three cases, i.e.,

1. when the train is located before the tunnel by $1R$,
2. when the train is entering the tunnel by $0.5R$, and
3. when the train is coming out of the tunnel by $0.5R$.

All of the flow fields are divided into three blocks like the following ways. x-direction is consistent with that of the train driving, y-directions normal to the train surface, and z-direction taken from the symmetric vertical surface to the ground. The origin of coordinates is at the ground and center of the tunnel exit.

Three cases are calculated, i.e. case 1 consists of inside the tunnel, behind the tunnel including the train, and behind the tunnel wall (40×25×25, 90×25×25, 90×20×25), case 2 of left side of the tunnel, inside the tunnel, and behind the tunnel (20×44×25, 40×25×25, 70×44×25), and case 3 of left side of the tunnel, inside the tunnel, and behind the tunnel (45×44×25, 40×25×25, 35×44×25). These sizes of grid guarantee the grid-independent solutions. Especially, the smallest grid spacings near to the solid wall are chosen to satisfy $y^+ < 5$, where $y^+ = \frac{y}{\nu}\sqrt{\frac{\tau_w}{\rho}}$.

The grid systems with the multi-blocks are effectively and easily generated using the GENIE++ [22] which is developed on the base of INGRID [20] and GENIE [21]. Figure I shows three distinct grid systems for each case.

4. Grid adaptation

The computational fluid dynamics (CFD) is mostly used to solve the flow field known or unknown by the experiments, and its accuracy depends not only on the solution algorithm to treat the governing equations but on the grid system. For example, it is difficult to capture the location of shock wave accurately in the compressible flow under the restriction of the grid size even though the solution procedures work very well, and thus the correct solution may not be obtained using the classical grid system. The concept and necessity of the adaptive grid have been stemmed from that, in other words, it is desirable to make the grids depending on the solution behavior such the ways as the dense grid in large gradient of solution and the sparse grid in small gradient of solution. The adaptive grid can be obtained by the redistribution [11, 13, 30], refinement [2, 28] or solution order increase; the first method adjust basically the grid spacing due to the solution gradient without changing the number of grids and may result in skewed grids, in the second one grid points are added locally in the region with large solution gradient, and the third one uses the higher order solution algorithm in the area with large solution gradient without changing the original grid system. The redistribution grid can be generated through the optimization, algebraic or partial differential method. The optimization method [28], based on the variational theory and iterative gradient optimization procedure, gives generally the smooth, nearly orthogonal adapted grid but it needs more time consumption.

The algebraic method [11–13, 31] easily generates the concentrated grid, which may not maintain the smoothness or orthogonality. Finally, the partial differential method [25] is similar to the optimization one in view of using the variational approach, but it should solve additionally the Euler–Lagrange equations. The method based on the algebraic procedure is partially used to generate the adaptive grids. The general and distinguished features embedded are as follows:

1. it can generate three-dimensional adapted grid based on surface-by-surface algebraic method with scaling the weight function,

2. the subsection concept (not multi-block) is introduced to scale the weight function and to treat the specified regions individually,

3. Non-Uniform Rational B-Spline (NURBS) interpolation, reparameterized uniform B-spline and transfinite interpolation are adopted to redistribute the adapted grid, to retain the sharp corners in the grid, and to remove the discontinuities between the subsections, respectively,

4. the diffusion concept is applied to obtain the local smoothness,

5. the local clustering, local orthogonality and solution interpolation are also available.

The weight factors which play a role to allot each weight to solutions or flow variables – pressure, velocities, density, temperature, etc. – should be given regardless of the choice of adaptation methods. It is suggested in this research to determine the weights and adaptation direction. The weight function is taken by

$$W = [1 + (\Sigma\lambda_j w_j) w_f] d_f, \qquad \Sigma\lambda_j = 1, \tag{12}$$

where w_j is a Boolean sum of solution gradient and curvature, λ_j the solution weight factor associated with flow parameter, w_f the weight factor to enhance the total effect, and d_f the distribution factor to generate weights. A Boolean sum w is defined by

$$w = \alpha q \oplus \beta k = \alpha q + \beta k + (1 - \alpha - \beta) qk, \tag{13}$$

where q and k are the scaled gradient and curvature of the flow variable, respectively, and α and β holding between 0 and 1 are parameters to be specified like that the grids are concentrated in the region of high gradients and large curvatures, and can be determined analytically [24, 31]. The chosen solutions are three velocity components, pressure and vorticity in this study.

The solution weight factor λ_j can be evaluated by Eq. (13) on the basis that the more change in flow parameters the more weight is allotted,

$$\lambda_j = \frac{\omega_j}{\sum_i \omega_i}, \qquad \omega_j = \sum_i \left| \frac{\partial \tilde{f}_j}{\partial x_i} \right|, \tag{14}$$

where $\tilde{}$ means the locally normalized value of solution. Even though the present method can generate the adapted grid generally and efficiently, it may have some restriction to be applied in three-dimensional flow field which contains the severe change in geometry or singularities. To avoid

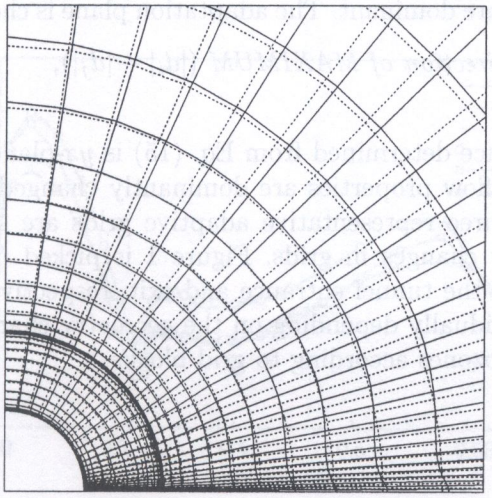

Fig. 1. Comparison of the original and adapted grids at $x/R = 4.97$ (case 1); solid: adapted, dotted: original

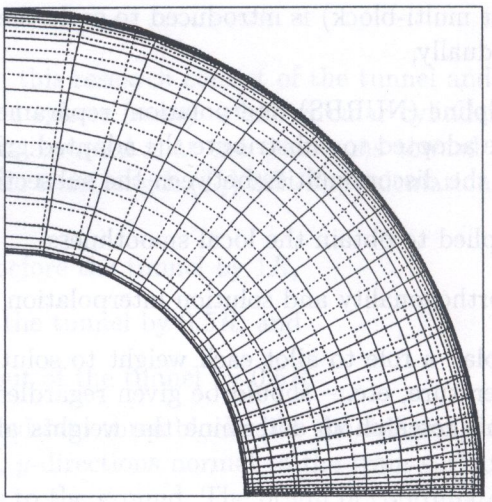

Fig. 2. Comparison of the original and adapted grids at $x/R = 3.0$ (case 2); solid: adapted, dotted: original

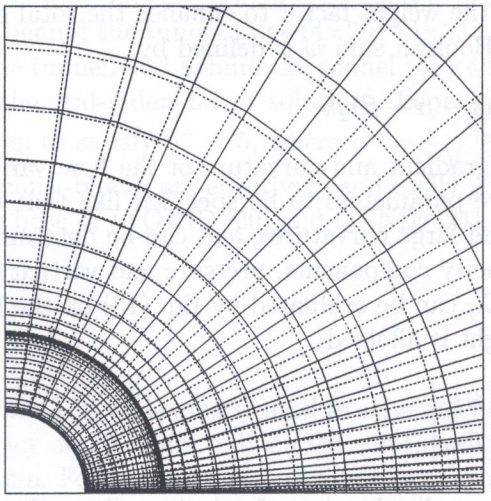

Fig. 3. Comparison of the original and adapted grids at $x/R = 0$ (case 3); solid: adapted, dotted: original

this disadvantage, the adaptation needs to be executed on the principal plane (or along the constant axis) where solution gradients are dominant. The adaptation plane is chosen by the following criteria,

$$\textit{direction of adaptation} = \textit{direction of MAXIMUM } (|d_i| + |d_j|), \tag{15}$$

where $d_i = \sum_k |\partial \tilde{f}_k / \partial x_i|$.

The principal adapted surface determined from Eq. (15) is yz-plane, i.e., x =constant plane for three cases all. It means that flow properties are dominantly changed on the plane normal to the direction of the main flow. Three representative adaptive grids are shown in Figs. 1–3, where it is found that there are pretty changes in grids. Figure 1 is picked up at the mid-section of the train, and Figs. 2 and 3 are at the tunnel entrance and exit, respectively. This method can handle the region to be adapted individually depending on the geometry characteristics, and so the whole region is divided into three subzones according to grid blocks.

5. Computation results

It is assumed that the train does not experience the ground effect, i.e., there is no gap between the train and ground. There is no flow separation around the train in this calculation, and the complete

vortex pair is not found around and behind the train. Figures 4–7 show the pressure distributions on the train surface according to the azimuthal angle Φ (measured from the symmetric plane toward the ground), where $X = (x - x_0)/L_t$ and x_0 is the location of the train nose. Comparing the body in the pure external flow, the train head and tail meeting the ground are considered likely as the stagnation point neglecting the effect induced by the ground. The pressure increases from the front nose and then decreases in the train head region because the flow is accelerated, and the reverse phenomena is found in its tail. It is easy to find in Fig. 7 that the pressure distributions are similar each other when the train enters and leaves the tunnel (case 2 and 3). Especially, the pressure distributions near the tunnel entrance and exit are different comparing that of case 1, in other words, the pressure on the train surface is influenced when it just passes the two locations, entrance and exit. The pressure distribution obtained from the adapted grid appears a little bit larger in the train head and smaller in its tail than that calculated from the original grid. The pressure on the surface generally decreases as Φ increases except near the tail. Figure II shows schematically that the surface pressure is high not only near the train nose but also just before its tail. Especially the same pressure regions in case 2 and 3 appear to be banded just before the train nose due to the influence of tunnel entrance and exit, and the pressure in the central region of the body part is higher than that in the side. Figures 8–11 show the skin friction distribution on the train surface. It is found that there are significant differences in skin friction distributions between the adapted solution and the non-adapted one in contrast to the pressure distribution. Regardless of the relative

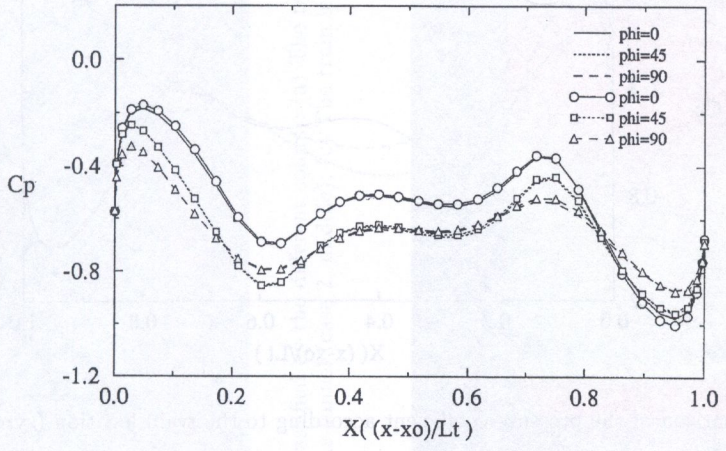

Fig. 4. Comparison of the pressure coefficient in case 1 (symbols: adapted)

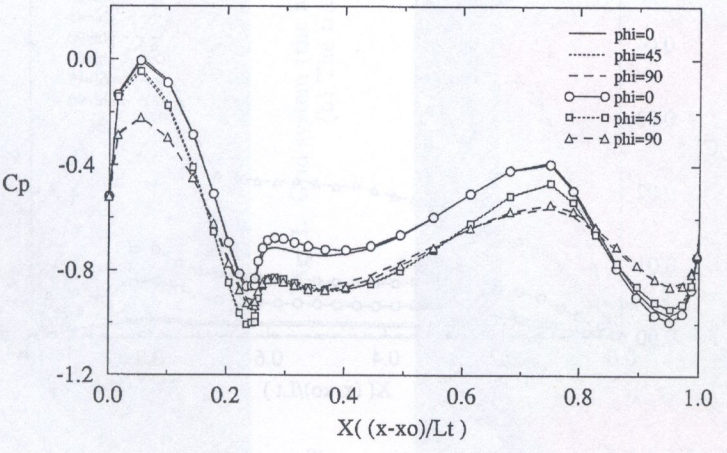

Fig. 5. Comparison of the pressure coefficient in case 2 (symbols: adapted)

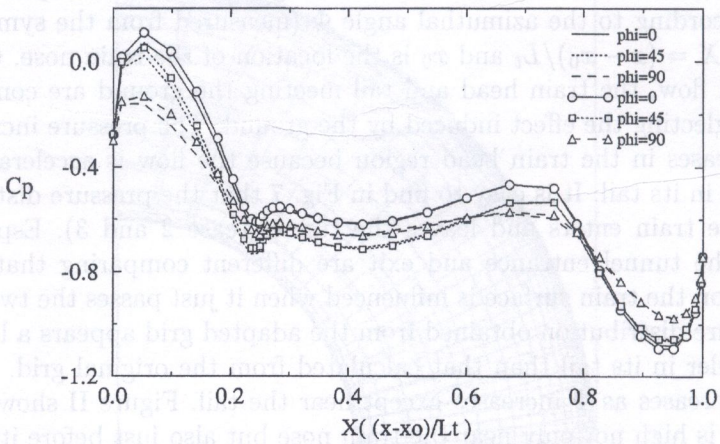

Fig. 6. Comparison of the pressure coefficient in case 3 (symbols: adapted)

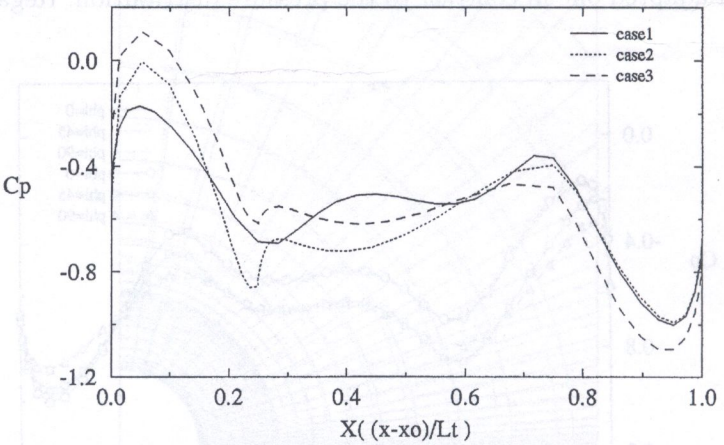

Fig. 7. Comparison of the pressure coefficient according to the train location (symbols: adapted)

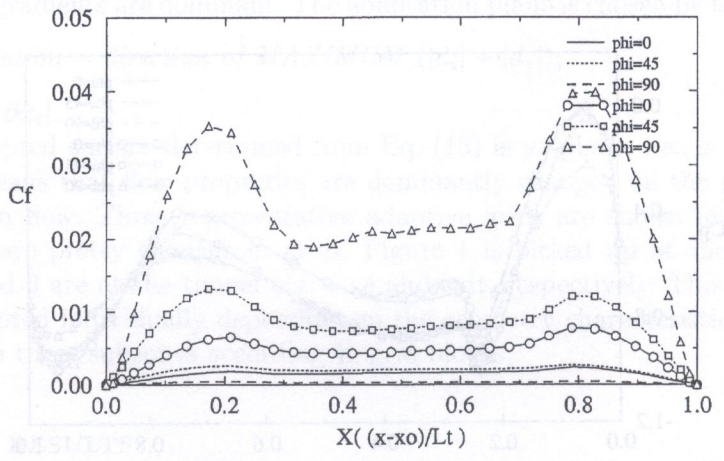

Fig. 8. Comparison of the skin friction coefficient in case 1 (symbols: adapted)

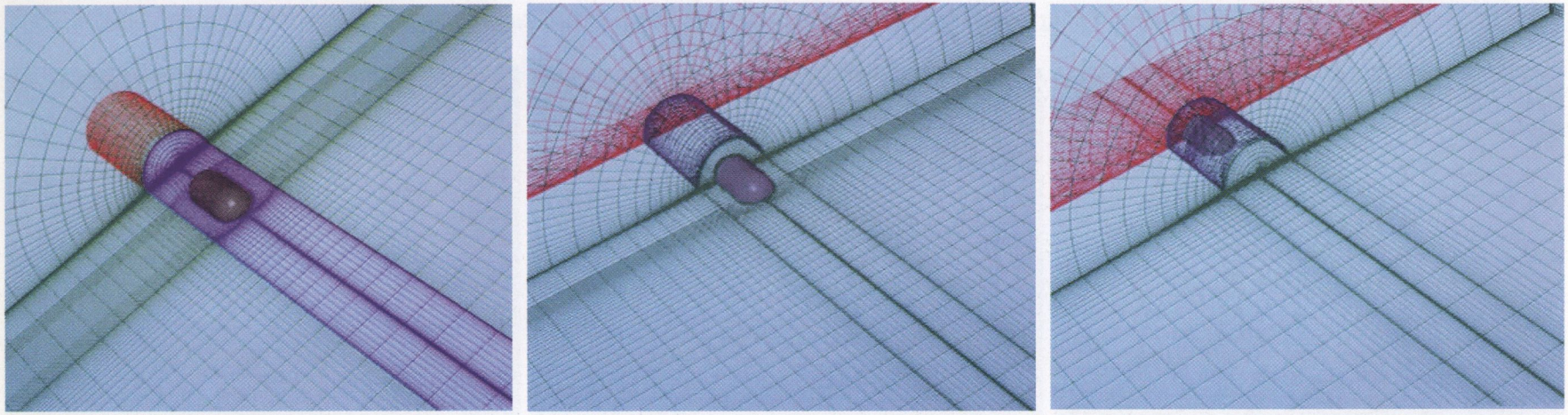

Fig. I. Grid system (the blocks are classified by the different colors): (a) The train locates in front of the tunnel (case 1, left); (b) The train enters the tunnel (case 2, middle); (c) The train leaves the tunnel (case 3, right)

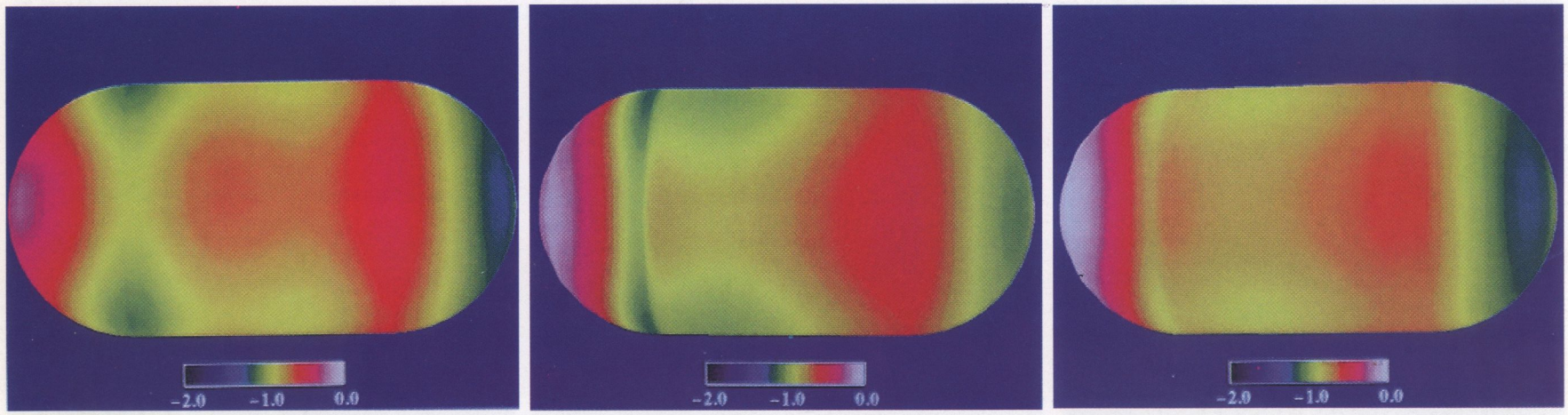

Fig. II. Pressure distribution on the train surface (case 1, 2 and 3 from left to right)

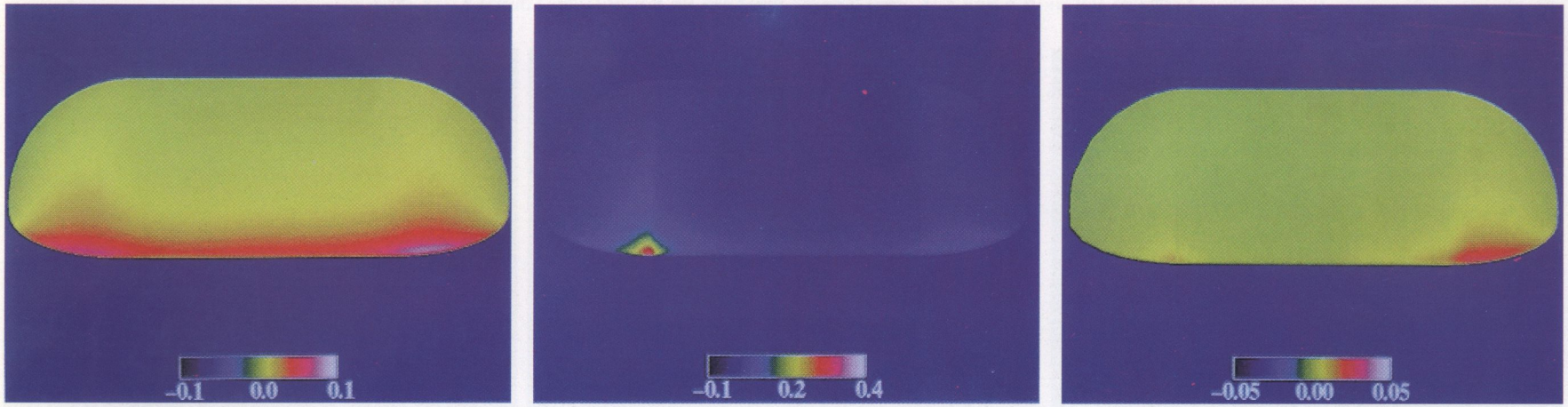

Fig. III. Distribution of the skin friction coefficient (case 1, 2 and 3 from left to right)

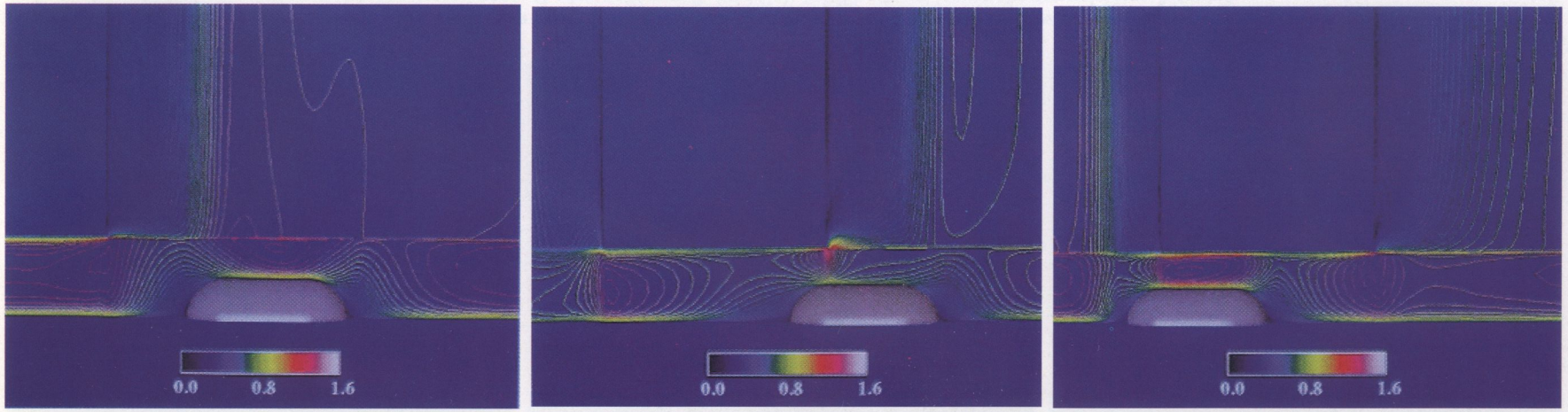

Fig. IV. Velocity magnitude on the symmetric plane (case 1, 2 and 3 from left to right)

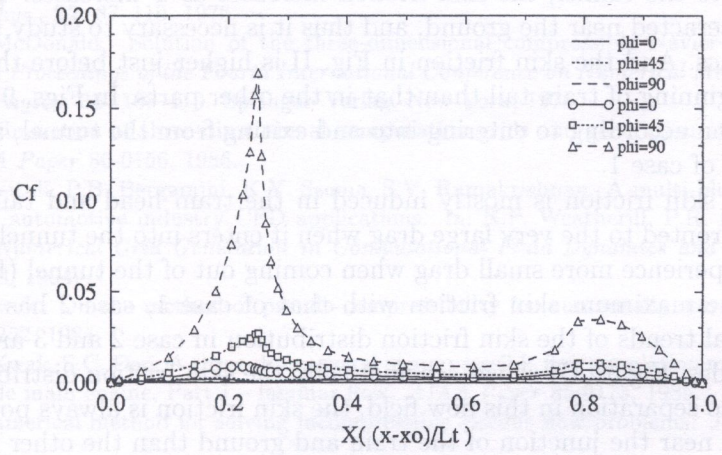

Fig. 9. Comparison of the skin friction coefficient in case 2 (symbols: adapted)

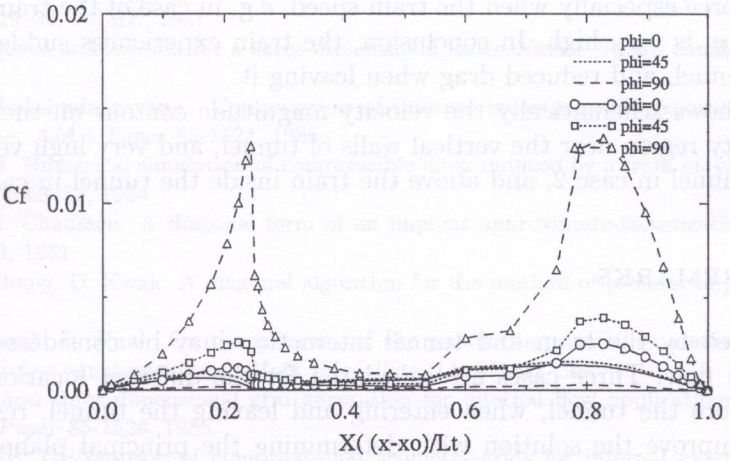

Fig. 10. Comparison of the skin friction coefficient in case 3 (symbols: adapted)

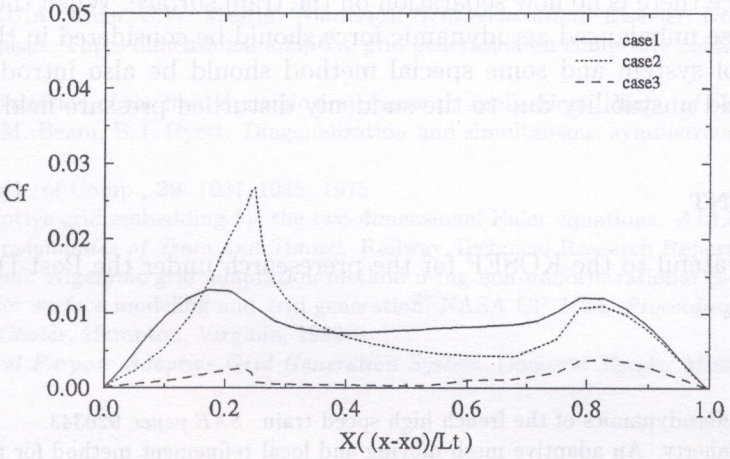

Fig. 11. Comparison of the skin friction coefficient according to the train location (symbols: adapted)

location of the train to the tunnel, the skin friction increases as Φ increases. This means that the flow field is highly interacted near the ground, and thus it is necessary to study the ground effect on the train aerodynamics. And the skin friction in Fig. II is higher just before the end of train head and just after the beginning of train tail than that in the other parts. In Figs. 9–10, there are sharp rises of the skin friction according to entering into and exiting from the tunnel, and this phenomena is different from that of case 1.

Thus drag by the skin friction is mostly induced in the train head and tail parts, ad hoc, the train is suddenly confronted to the very large drag when it enters into the tunnel, in contrast to this, the train comes to experience more small drag when coming out of the tunnel (Fig. 11). Comparing the magnitudes of the maximum skin friction with that of case 1, case 2 has 5 times and case 3 1/3 times. The general trends of the skin friction distribution in case 2 and 3 are similar each other except their magnitudes. Figure III shows schematically the skin friction distributions for the three cases. Since there is no separation in this flow field, the skin friction is always positive. In case 1, the skin friction is higher near the junction of the train and ground than the other parts, and in case 2 and 3, more higher skin friction is induced near the entrance and exit of the tunnel. As mentioned above, the train is under the very high skin friction condition when it enters into the tunnel. These drastic aerodynamic forces induced by the direct interaction of the tunnel have an influence on the stability of the train, thus the concept of driving control should be introduced to compensate the drastic unbalanced force especially when the train speed, e.g. in case of the train floated and driven by the magnetic force, is very high. In conclusion, the train experiences suddenly very large drag when entering the tunnel, and reduced drag when leaving it.

Finally, Fig. IV shows schematically the velocity magnitude contour on the symmetric surface. There is small velocity region near the vertical walls of tunnel, and very high velocity is found near the right corner of tunnel in case 2, and above the train inside the tunnel in case 3.

6. Concluding remarks

The flow field induced by the train and tunnel interaction may be considered as an example of the internal–external flow. Three cases are calculated for the different locations of the simplified train shape, i.e., before the tunnel, when entering and leaving the tunnel, respectively. And the grid is adapted to improve the solution with determining the principal plane on which the flow variables are changed dominantly. When the train enters into the tunnel, the pressure distribution in the train head and the skin friction distribution both in the train head and tail are severely high comparing with the other cases, and thus the unsteady aerodynamic force is acting. Pressure is higher in the train head than in its tail, so the positive pressure drag is formed, and the skin friction is always positive since there is no flow separation on the train surface. When the high speed surface train is designed, these unbalanced aerodynamic force should be considered in the design procedure of the driving control system and some special method should be also introduced to reduce the aerodynamic noise and unstability due to the suddenly disturbed pressure field.

Acknowledgment

The first author is grateful to the KOSEF for the preresearch under the Post-Doc. program.

References

[1] S. Aita *et al.* CFD Aerodynamics of the french high speed train. *SAE paper* 920343.

[2] D.C. Arney, J.E. Flaherty. An adaptive mesh-moving and local refinement method for time-dependent partial differential equations. *ACM Trans. on Math. Software*, **16**(1): 48–71, 1990.

[3] B.S. Baldwin, H. Lomax. Thin layer approximation and algebraic model for separated turbulence flows. *AIAA Paper* 78-0257, 1978.

[4] R.M. Beam, R.F. Warming. An implicit finite-difference algorithm for hyperbolic system in conservation-law form. *J. Comp. Phys.*, **22**: 87–110, 1976.

[5] W.R. Briley, H. McDonald. Solution of the three-dimensional compressible Navier–Stokes equations by an implicit technique. *Proceedings of the Fourth International Conference on Numerical Methods in Fluid Dynamics, Lecture Notes in Physics* **35**, 105–110. Springer–Verlag, New York, 1975.

[6] R. Carcaillet. Optimization of three-dimensional computation grids and generation of flow adaptive computational grids. *AIAA Paper* 86-0156, 1986.

[7] M. Casella, D.F. Vitali, P.B. Bergamini, K.Y. Szema, S.V. Ramakrishnan. A multi-block structured grid interactive package for automotive industry CFD applications. In: N.P. Weatherill, P.R. Eiseman, J. Hauser, J.F. Thompson, eds., *Numerical Grid Generation in Computational Fluid Dynamics and Related Fields,* 403–415. Pineridge, England, 1994.

[8] J.L. Chang, D. Kwak. On the method of pseudo-compressibility for numerically solving incompressible flows. *AIAA Paper* 84-0252, 1984.

[9] J.L.C. Chang, D. Kwak, S.C. Dao. A three-dimensional incompressible flow simulation method and its application to the space shuttle main engine, Part I – laminar flow. *AIAA Paper* 85-0175, 1985.

[10] A.J. Chorin. A numerical method for solving incompressible viscous flow problems. *J. Comp. Phys.*, **2**: 12–26, 1967.

[11] W.C. Connett, R.K. Agarwal, A.L.Schwartz. An adaptive grid-generation scheme for flow field calculations. *AIAA Paper* 87-0199, 1987.

[12] C.B. Davies, E.Venkatapathy. Application of a solution adaptive grid scheme, SAGE, to complex three-dimensional flows. *AIAA Paper* 91-1594, 1991.

[13] P.R. Eiseman. Adaptive grid generation by mean value relaxation. In: K.N. Chia, U. Chia, eds., *Advances in Grid Generation*, 29–34. ASME, 1981.

[14] J. Flores. Convergence acceleration for a three-dimensional Euler/Navier–Stokes zonal approach. *AIAA Paper* 85-1495, 1985.

[15] K.R. Kirtley, B. Lakshminarayana. Computation of internal incompressible separated flows using a space-marching technique. *AIAA Paper* 85-1624, 1985.

[16] T. Ogawa, K. Fujii. Numerical simulation of compressible flows induced by a train moving into a tunnel. *Comp. Fluid Dyn. J.*, **3**(1): 63–82, 1994.

[17] T.H. Pulliam, D.S. Chaussee. A diagonal form of an implicit approximate-factorization algorithm. *J. Comp. Phys.*, **39**: 347–363, 1981.

[18] S.E. Roger, J.L. Chang, D. Kwak. A diagonal algorithm for the method of pseudocompressibility. *AIAA Paper* 86-1060, 1986.

[19] S.E. Rogers, D. Kwak, U. Kaul. On the accuracy of the pseudocompressibility method in solving the incompressible Navier–Stokes equations. *Appl. Math. Modelling*, **11**: 35–44, 1987.

[20] B.K. Soni. Two- and three-dimensional grid generation for internal flow applications of computational fluid dynamics. *AIAA Paper* 85-1526, 1985.

[21] B.K. Soni. GENIE: GENeration of computational geometry-grids for internal–external flow configurations. *Proceedings of the Numerical Grid Generation in Computational Fluid Mechanics'88, Miami, FL*, 1988.

[22] B.K. Soni, J.F. Thompson, M. Stokes, M.-S. Shih. GENIE++, EAGLEView and TIGER: General and special purpose interactive grid systems. *AIAA Paper* 92-0071, 1992.

[23] M. Swarden. *Vehicle Tunnel Entry at Subsonic Speeds, Final Report.* DSR 76111-4, US Department of Transportation, Jan. 1973.

[24] J.F. Thompson, Z.U.A. Warsi, C.W. Mastin. *Numerical Grid Generation.* Elsevier, North-Holland, 1985.

[25] Y. Tu, J.F. Thompson. Three-dimensional adaptive grid generation on composite configurations. *AIAA J.*, **29**: 20–25, 1991.

[26] E. Turkel. Symmetrization of the fluid dynamic matrices with applications. *Math. of Comp.*, **27**: 729–736, 1973.

[27] R.F. Warming, R.M. Beam, B.J. Hyett. Diagonalization and simultaneous symmetrization of the gas dynamic matrices.
emphnewblock Math. of Comp., **29**: 1037–1045, 1975.

[28] G.P. Warren. Adaptive grid embedding for the two-dimensional Euler equations. *AIAA Paper* 90-3049, 1990.

[29] A. Yamamoto. *Aerodynamics of Train and Tunnel.* Railway Technical Research Report No. 1230, 1983.

[30] J.C. Yang, B.K. Soni. Algebraic grid adaptation method using non-uniform rational B-spline surface modeling; Software systems for surface modeling and grid generation. NASA CP 3134, *Proceedings of a Workshop held at Langley Research Center,* Hampton, Virginia, 1992.

[31] J.-C. Yang. *General Purpose Adaptive Grid Generation System,* Doctoral Thesis. Mississippi State University, 1993.